

See discussions, stats, and author profiles for this publication at: <https://www.researchgate.net/publication/263946504>

p-Type Doping of Spiro-MeOTAD with WO₃ and the Spiro-MeOTAD/WO₃ Interface Investigated by Synchrotron-Induced Photoelectron Spectroscopy

ARTICLE *in* THE JOURNAL OF PHYSICAL CHEMISTRY C · AUGUST 2012

Impact Factor: 4.77 · DOI: 10.1021/jp301179v

CITATIONS

12

READS

74

3 AUTHORS, INCLUDING:



Thomas Mayer

Technical University Darmstadt

94 PUBLICATIONS 1,099 CITATIONS

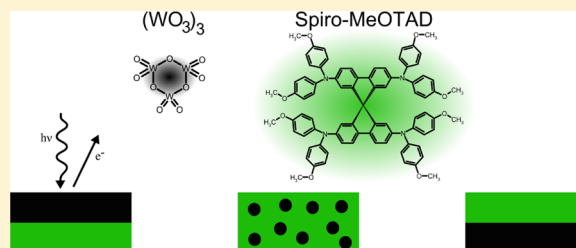
SEE PROFILE

p-Type Doping of Spiro-MeOTAD with WO₃ and the Spiro-MeOTAD/WO₃ Interface Investigated by Synchrotron-Induced Photoelectron Spectroscopy

René Hock,[†] Thomas Mayer,^{*,†} and Wolfram Jaegermann^{†,‡}[†]Fachbereich Materialwissenschaft, Petersenstrasse 32, Technische Universität Darmstadt, 64287 Darmstadt, Germany[‡]Center of Smart Interfaces, Petersenstrasse 32, Technische Universität Darmstadt, 64287 Darmstadt, Germany

ABSTRACT: p-Doping of the organic hole conductor Spiro-MeOTAD with tungsten oxide (WO₃) is investigated by synchrotron-induced photoelectron spectroscopy (SXPS). Similar valence band spectra and electronic-state energies are shown for Spiro-MeOTAD films evaporated in UHV and prepared by drop-casting from cyclohexanone solution. In coevaporated Spiro-MeOTAD:WO₃ films with varying amounts of WO₃, a maximum shift of the HOMO binding energy by 0.98 eV toward the Fermi level is found. Similar shifts are induced in Spiro-MeOTAD at interfaces of Spiro-MeOTAD on WO₃ and WO₃ on Spiro-MeOTAD.

In addition, interface dipole potentials of 0.87 and 1.36 eV, respectively, are induced in the two deposition sequences. The exchanged charge appears as a reduced W⁵⁺ component in W4f core orbital and additional W5d gap-state emissions. A correlation of the interface charge transfer to the doping mechanism is discussed.



INTRODUCTION

In general, the concept of doping is not only employed for inorganic semiconductors but is also increasingly important in the field of organic electronics. For example, in heterojunction solar cells, doping can lead to improvements in power conversion efficiencies by a factor of nearly 2.¹

Solid-state hole-conducting spiro molecules, such as the investigated 2,2',7,7'-tetrakis(*N,N*-di-*p*-methoxyphenylamine)-9,9'-spirobifluorene (Spiro-MeOTAD), are currently under investigation as a solid-state replacement for the liquid triiodide/iodide electrolyte employed in dye-sensitized solar cells (DSSC). The spiro center is the tetrahedral-coordinated, sp³-hybridized C-atom which combines two π -systems.^{2–4} The perpendicular, cross-shaped structure of the spiro-linked molecules minimizes the intermolecular interactions responsible for aggregation in the solid-state, which causes entanglement and thus hinders recrystallization, and improves the solubility compared to the nonspiro parent compounds.⁵

In solid-state DSSC, Li-salts and other additives are added as dopants to the dissolved Spiro-MeOTAD to enhance the intrinsically poor conductivity and thus the efficiency of the DSSC.⁶ Another approach of the p-type doping of organic semiconductors is the codeposition of transition metal oxides, such as WO₃ and MoO₃. This was already shown for different semiconducting molecules.^{7–10} As a possible doping mechanism, an energetically favored electron transfer from the HOMO of the organic molecule to the unoccupied states of the oxide, namely the conduction band, is discussed.

In this work, Spiro-MeOTAD and WO₃ are coevaporated to investigate systematically the p-doping and the doping limit. Charge transfer and the doping mechanism as well as the

function of WO₃ in contact with Spiro-MeOTAD as a hole injection layer are investigated by interface experiments of Spiro-MeOTAD on WO₃ and WO₃ on Spiro-MeOTAD. Band diagrams of the pristine materials and of the heterocontacts are derived. In addition, it is shown that the valence band spectra of drop-casted and vacuum-deposited Spiro-MeOTAD films appear almost identical.

EXPERIMENTAL SECTION

Thin film samples were prepared by stepwise evaporation of powder materials from homemade effusion cells in an ultrahigh vacuum chamber with a base pressure of 10^{−9} mbar. Deposition rates of Spiro-MeOTAD and WO₃ were approximately 0.3 Å/s for the interface experiments and varied during coadsorption experiments according to the desired doping concentration. All film thicknesses as well as the deposition rates were determined by the damping of the respective substrate emission lines. Drop-casted films of Spiro-MeOTAD were prepared from cyclohexanone (>99%) solution in a glass cell directly attached to the UHV system, which was rinsed with pure argon (5.0) and allowed the transfer of the samples to vacuum without contact to ambient air. Dense TiO₂ blocking layers on top of a FTO film obtained from BASF were used as substrates. Spiro-MeOTAD (>99%) was purchased from Lumtec and WO₃ powder (99.9%) from Sigma Aldrich. Synchrotron-induced photoelectron spectroscopy (SXPS) of interfaces and codepos-

Received: February 6, 2012

Revised: July 13, 2012

Published: July 17, 2012



ited and drop-casted films were performed in a Solid Liquid Analysis System (SoLiAS) at the synchrotron light source BESSY II in Berlin at the beamlines U49/2-PGM2 and TGM7. All spectra were recorded with a SPECS Phoibos 150 hemispherical analyzer under a base pressure of 10^{-10} mbar. In the photon energy range from 90 to 600 eV at the U49/2-PGM2 and from 47 to 120 eV at the TGM7, the obtained resolution, determined by the fwhm of the Fermi-edge at room temperature, was in the range of 180–240 meV depending on the excitation energy. The binding energy scale was calibrated against the Fermi-edge of a silver standard. Work functions were derived from the secondary electron edge position, which was measured with an applied bias voltage of 6 eV. Binding energy positions were derived from a fit of the photoemission lines using Gauss–Lorentz mixed Voigt profile after Shirley-background subtraction.¹¹ The binding energy values of the HOMO states are referred to the emission maxima in contrast to the onset as used in general in the organic electronics literature. Binding energy values are given to the 0.01 eV digit, which we use to determine relative changes. The absolute positions should be rounded up to the closest 0.1 eV digit.

RESULTS

Pristine Materials. Spiro-MeOTAD. To test the effect of the deposition process on the electronic-state distribution, films of pristine Spiro-MeOTAD are prepared by drop-casting and by evaporation. The striking coincidence of the extremely sensitive valence band spectra displayed in Figure 1 demonstrate the equivalency of the two deposition processes. The work function is measured to be 4.2 eV in both cases. According to the theoretical calculated density of states of the

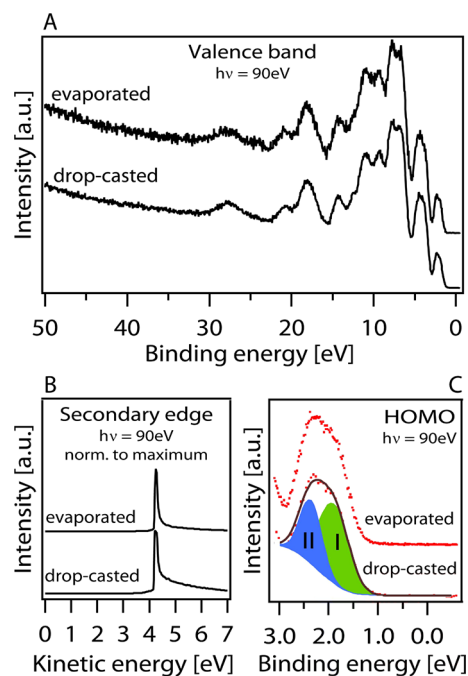


Figure 1. Valence band (A), secondary edge (B), and HOMO (C) measurements of drop-casted and in situ-evaporated Spiro-MeOTAD. The striking similarity demonstrates the electronic equivalency of the films formed by the different deposition techniques. The work function is 4.2 eV. The HOMO emission is decomposed into HOMO (I) at 1.87 and HOMO-1 (II) at 2.27 eV. All spectra were recorded with 90 eV photon energy.

HOMO orbitals of Spiro-6P and Spiro-PBD performed by Johansson et al.,⁴ the valence peak with the lowest binding energy consists of HOMO and HOMO-1, separated by ca. 0.3 eV. The fitted binding energies of the emission maxima of the molecular orbitals of the respective valence peak of undoped Spiro-MeOTAD are 1.87 and 2.27 eV (labeled as “I” and “II” in Figure 1C) for both deposition processes. Also the C1s core level emissions illustrated in Figure 2 show the same curve form

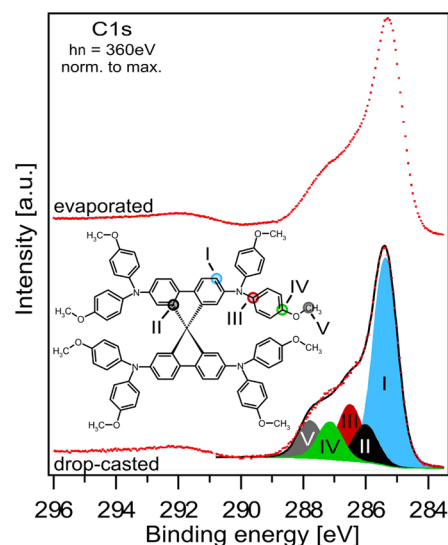


Figure 2. C1s emission of evaporated and drop-casted Spiro-MeOTAD taken at 360 eV photon energy. Decomposition into emissions assigned to (I-blue) C–H at 285.37 eV, (II-black) spiro C–C at 286.01 eV, (III-red) C–N at 286.50 eV, (IV-green) aromatic C–O at 287.14 eV, and (V-gray) C–O at 287.78 eV is indicated. The relative intensities are chosen according to stoichiometry.

and similar binding energies of 285.25 and 285.39 eV for the drop-casted and evaporated film, respectively. In Figure 2, the C1s core level spectrum is fitted with five emission lines assigned to chemically shifted carbon species according to the different carbon bonds in the molecule. The intensities are chosen according to the stoichiometry of the molecule. The different emission lines are attributed to C–H at 285.37 eV, spiro C–C at 286.01 eV, C–N at 286.50 eV, aromatic C–O at 287.14 eV, and C–O at 287.78 eV.

WO₃. Dense films of WO₃ (25 nm) were deposited on Spiro-MeOTAD and on TiO₂ substrates. The valence band and the low-lying O2s and W4f core levels measured with 90 eV photon energy are displayed in Figure 3A. The WO₃ film on the TiO₂ substrate shows a stronger gap-state emission (Figure 3C) with a maximum at 0.8 eV binding energy and a stronger W4f component shifted by 1.2 eV to low binding energy with respect to the main emission assigned to W⁶⁺ of stoichiometric WO₃. Similar gap state and core level emissions have been measured previously on WO₃(001) surfaces and were related to oxygen defects causing occupation of the W5d orbital of neighbor W atoms that appear as reduced W⁵⁺ component in the W4f emission.^{12–14} The WO₃ valence band maxima of 3.24 eV on Spiro-MeOTAD and 3.33 eV on TiO₂ were determined as the onset of the valence band edge. The work function of WO₃ is 6.12 eV on TiO₂ and 6.76 eV on Spiro-MeOTAD as derived from the secondary emission edge (Figure 3B). The decreased value on TiO₂ may be correlated to induced oxygen defects and reduced W⁵⁺ species. To analyze the TiO₂/WO₃

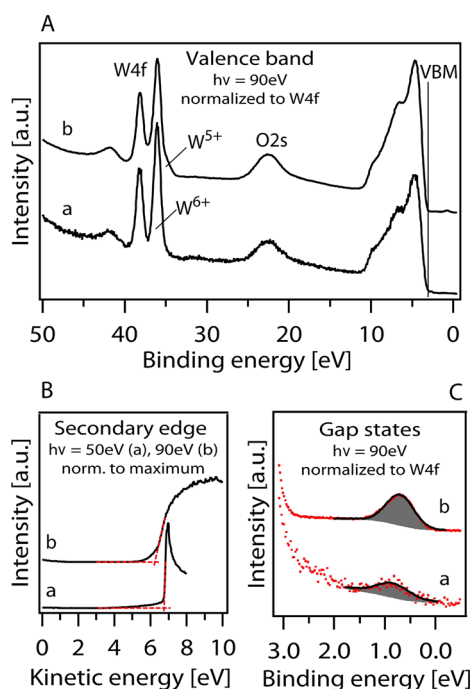


Figure 3. Valence band (A), secondary edge (B), and gap states (C) spectra of the in situ-evaporated WO_3 onto Spiro-MeOTAD (a) and on TiO_2 (b). On TiO_2 , increased W^{5+} and gap-state emissions are evident. Derived work function values are 6.76 (a) and 6.12 eV (b). Valence band spectra, gap-state spectra, and secondary edge (a) with 50 eV.

interface formation, WO_3 was stepwise deposited onto TiO_2 blocking layers used in the solid-state DSSC to inhibit contact between the FTO electrode and Spiro-MeOTAD. Measurements of both nanocrystalline TiO_2 and TiO_2 blocking layers showed electrical equivalency, concerning valence band spectra, gap-state distribution, and work function, as shown by Schwanitz et al.¹⁵ In Figure 4, the changes in the W4f emission (left) and Ti2p emission (right) are displayed. The TiO_2 substrate shows a Ti2p component shifted to a lower binding energy assigned to reduced Ti^{3+} and a gap-state emission assigned to occupied Ti3d states (not shown) due to oxygen defects.¹⁶ With WO_3 deposition, the Ti^{3+} emission disappears while the reduced W^{5+} component is strongest at the

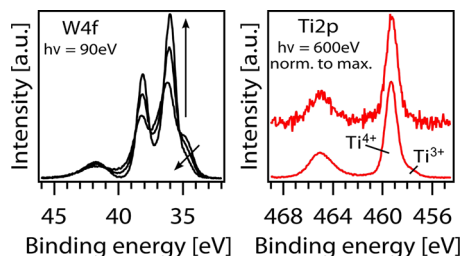


Figure 4. W4f spectra for three steps of WO_3 deposition onto TiO_2 and Ti2p spectra for the second step of WO_3 deposition onto TiO_2 , taken at 90 and 600 eV photon energy, respectively. The W4f emission shoulder at a lower binding energy is assigned to W^{5+} and the low energy shoulder in Ti2p to Ti^{3+} due to oxygen defects. The W^{5+} emission is strong in the first step while Ti^{3+} disappears, indicating breaking of the W–O bond in tungsten oxide and Ti–O formation in oxygen-defective titanium oxide. W4f is shown as measured, and Ti2p is normalized to the intensity maximum.

interface and decreases with increasing WO_3 thickness. Thus, we can conclude that at the TiO_2/WO_3 interface, oxygen-defective titanium becomes oxidized while tungsten oxide, which is assumed to evaporate as W_3O_9 clusters,¹⁷ is reduced.

The electronic structure of pristine Spiro-MeOTAD and (marginally reduced) WO_3 films are compared in the vacuum level alignment, the so-called Anderson lineup in Figure 5. The

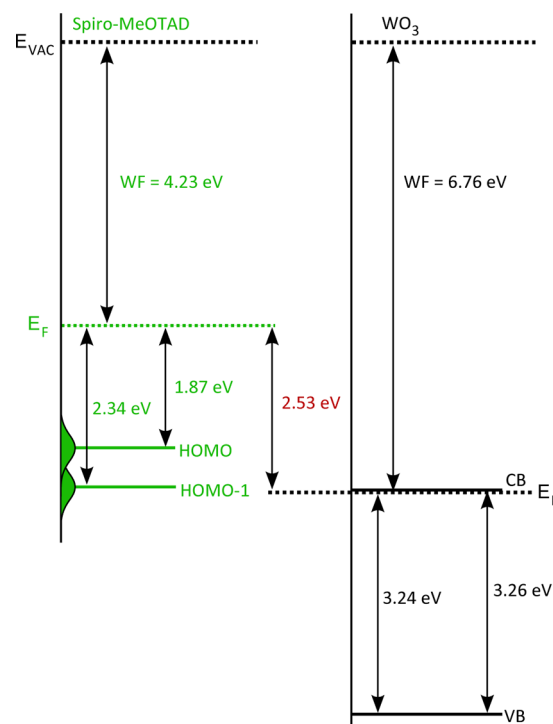


Figure 5. Comparison of the band diagrams in the vacuum level lineup of pristine Spiro-MeOTAD and pristine WO_3 on Spiro-MeOTAD (b in Figure 3) before contact. The HOMO binding energy values refer to the photoemission maximum position.

comparison shows the situation before contact, neglecting a possible interface dipole (see later), and visualizes the possible charge transfer from WO_3 to Spiro-MeOTAD. The band gap of WO_3 prepared in a vacuum PVD process depends on the substrate temperature at which the deposition was performed.¹⁸ At room temperature, the gap is 3.26 eV, which is related to amorphous WO_3 ^{18,19} which may contain crystalline precipitates.²⁰ Due to the high WO_3 electron affinity of 6.74 eV and work function of 6.76 eV compared to the low Spiro-MeOTAD ionization energy of 6.1 eV and work function of 4.2 eV, electron transfer from Spiro-MeOTAD to WO_3 can be expected at the WO_3 /Spiro-MeOTAD bilayer interface and in codeposited films.

Spiro-MeOTAD: WO_3 Composites. To investigate doping of Spiro-MeOTAD with WO_3 dense films (25 nm) of Spiro-MeOTAD: WO_3 composites with varying WO_3 content of 0.0%, 0.9%, 7%, 34%, 76%, and 100% have been prepared. As the measurements on the composites were performed at beamline TGM7 with maximum photon energy of 120 eV, the C1s core level could not be measured. The WO_3 content of the composites was estimated from the intensity fraction of WO_3 gap states to Spiro-MeOTAD HOMO emission. A gradual change from Spiro-MeOTAD to WO_3 spectral characteristics can be observed in Figures 6 and 7 where spectra from pristine Spiro-MeOTAD and WO_3 are presented together with the

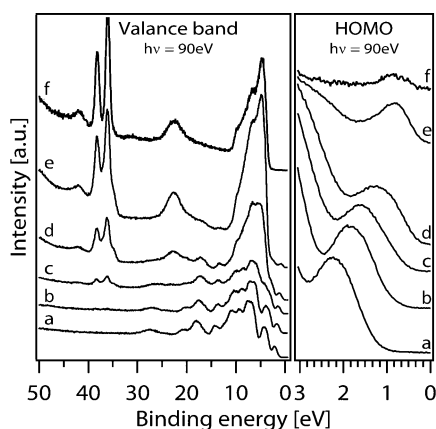


Figure 6. Valence band spectra of Spiro-MeOTAD:WO₃ composites taken at 90 eV photon energy: (a) pristine Spiro-MeOTAD, (b) 0.9%, (c) 7%, (d) 34%, and (e) 76% WO₃-content, (f) pristine WO₃. The Spiro-MeOTAD emissions shift to lower binding energy, as evidenced by the HOMO detailed spectra.

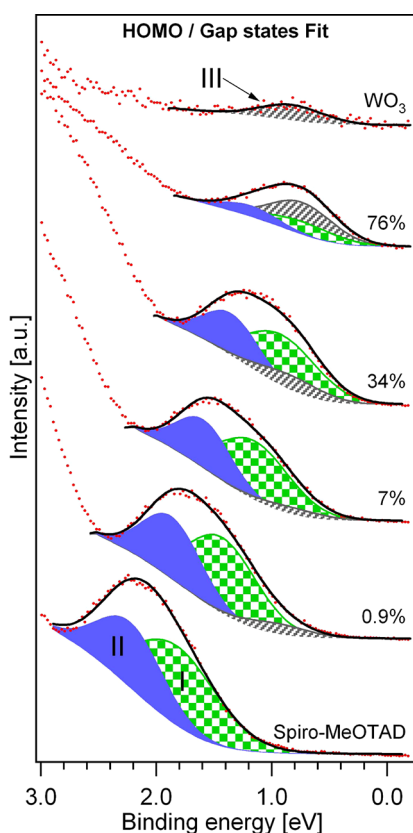


Figure 7. The decomposition of the HOMO and gap-state emissions of Spiro-MeOTAD:WO₃ composites of the indicated composition into HOMO (I-green), HOMO-I (II-blue), and WO₃ gap states (gray). The binding energy of WO₃ gap states was chosen assuming a fixed distance with respect to the W4f binding energy given in Figure 8. Intensity ratio and energy distance of HOMO and HOMO-I were kept constant.

composites. With increasing WO₃ content, the intensity of the W4f core level lines (~ 36 eV) and the WO₃ valence band structure increases. The HOMO of Spiro-MeOTAD shifts with increasing dopant content to lower binding energies (Figures 6, 7 and 9) up to 0.98 eV, proving the p-doping. Gap states of WO₃ (indexed as “III”) and the two HOMO orbitals of Spiro-

MeOTAD (indexed as “I” and “II”) both contribute to the features of the composites in the HOMO and gap-state region (Figure 7) measured at 90 eV photon energy. As relative positions and intensities of emissions from the two materials also change with the content of WO₃, the shape of the valence band and of the HOMO and gap-state region changes. For the fitting procedure, the binding energy distance of the WO₃ gap states and the W4f emission line of 35.28 eV, the energy distance of the Spiro-MeOTAD HOMO orbitals of 0.43 eV, and their intensity ratio of 0.83 were kept constant.

Figure 8 shows the Shirley background-subtracted W4f detail spectra of the composites and pristine WO₃. Fits were

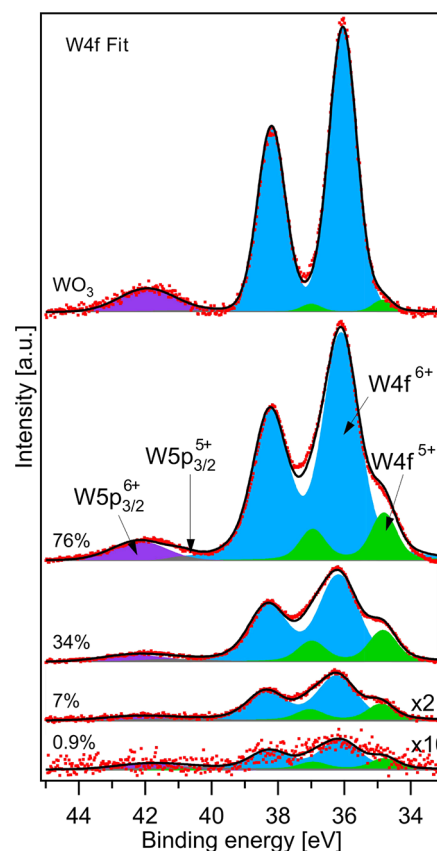


Figure 8. The W4f emission of Spiro:WO₃ composites with indicated WO₃ content and of pristine WO₃. Decomposition into W4f⁶⁺ (blue), W4f⁵⁺ (green), W5p_{3/2}⁶⁺ (lilac), and W5p_{3/2}⁵⁺ (gray) is indicated. The absolute intensity of the low binding energy component W⁵⁺ increases with the increasing WO₃ content. The W⁵⁺ intensity is very low for WO₃ on Spiro-MeOTAD (compare to Figure 3).

performed with a W4f_{5/2}/W4f_{7/2} doublet splitting of 2.15 eV²¹ and a fitted doublet intensity fraction W4f_{5/2}/W4f_{7/2} of 0.65. The branching ratio can deviate from the statistical one (0.75) because of, for example, discrepancies in the photo-excitation cross section and the availability of final states for different photon energies.²² All W4f spectra show a component located at approximately 1.3 eV lower binding energy with respect to the W⁶⁺ emission, which is attributed to a reduced species in the formal W⁵⁺ oxidation state. In addition to the W4f emission, also emission from the W5p orbital appears at approximately 42 eV and was fitted with two components for the 6+ and 5+ species shifted by ca. 1.3 eV as for W4f. The change of the W4f⁵⁺ to W4f⁶⁺ fraction and the Spiro-MeOTAD binding energy shift with an increasing WO₃ content is plotted

in Figure 9. The ratio between the $W4f^{5+}$ and $W4f^{6+}$ components of WO_3 is constant (0.26) up to approximately

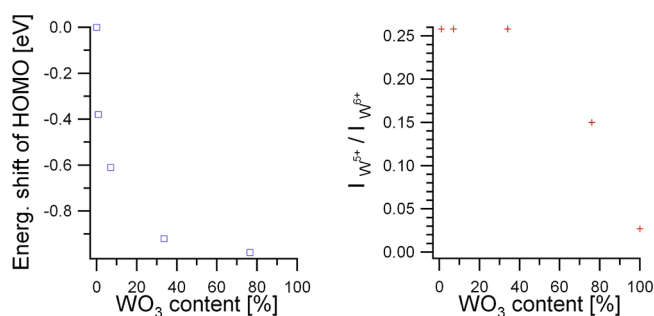


Figure 9. Shift of Spiro-MeOTAD HOMO binding energy in Spiro-MeOTAD: WO_3 composites and the W^{5+}/W^{6+} emission intensity ratio. The HOMO energy shift due to p-doping is strong in the first three steps and then levels off. While the absolute intensity of W^{5+} increases with WO_3 content, the relative intensity is constant in the first three steps and then decreases.

34% WO_3 content and decreases for higher contents. The HOMO shift increases strongly up to around 34% WO_3 content and saturates at 0.98 eV.

Interfaces. WO_3 /Spiro-MeOTAD. To investigate systematically the reduced $W4f$ species in the codeposited films and its possible correlation to charge transfer indicated by the binding energy shift of the Spiro-MeOTAD emissions in the codeposited films, interface experiments were performed. Spiro-MeOTAD was in situ-evaporated stepwise onto a dense and thick layer of WO_3 (25 nm) on a TiO_2 film. With increasing Spiro-MeOTAD thickness, the valence band spectra (Figure 10) show a shift of the HOMO of Spiro-MeOTAD of up to 1.12 eV to higher binding energies. The $W4f$, HOMO,

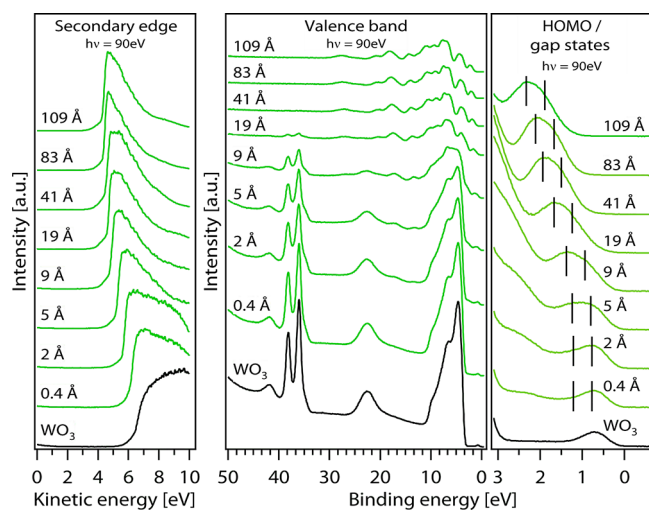


Figure 10. The secondary electron emission edge, valence band, and $W4f$ core level spectra as well as the detailed HOMO/gap-state region of WO_3 (bottom-black) and the stepwise evaporated Spiro-MeOTAD (green) of indicated thickness. The work function decreases until it reaches the value of pure Spiro-MeOTAD at 4.23 eV. The WO_3 features are damped while Spiro-MeOTAD features grow in intensity. The energy positions of the two HOMO-state maxima are marked. An upward band bending toward the interface is evident, indicating electron transfer to WO_3 . The spectra were recorded with a photon energy of 90 eV.

and gap-state emission features were fitted in the same way as described for the composites.

The work function decreases from 6.22 eV to the value of pure Spiro-MeOTAD of 4.23 eV. The $W4f$ emission is damped but not energetically shifted. The $W4f$ emission of the pure WO_3 film (Figure 11) shows a small binding energy shoulder

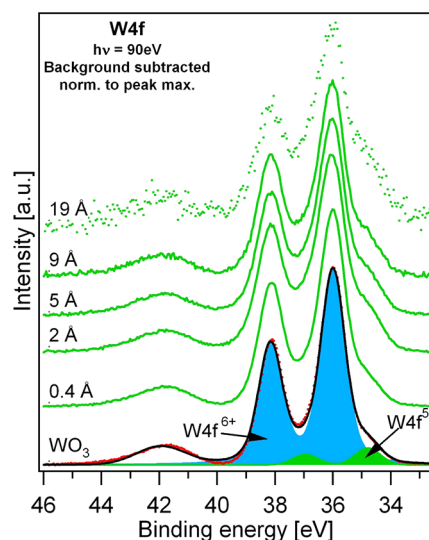


Figure 11. The integral intensity-normalized $W4f$ detailed spectra in the course of the Spiro-MeOTAD deposition (green) onto a WO_3 layer (bottom-black) on TiO_2 . Because of the oxidation by defective TiO_2 , $W4f^{5+}$ is present in the pristine WO_3 film (compare to Figure 3). The relative intensity of the low energy shoulder increases with growing Spiro-MeOTAD thickness. Spectra were recorded with 90 eV photon energy.

due to the oxidation of oxygen vacancies of the TiO_2 surface as described above. The relative intensity of the $W4f^{5+}$ position increases with increasing Spiro-MeOTAD thickness as evidenced in the Shirley background-subtracted detailed spectra normalized to $W4f^{6+}$. Figure 12 plots the relative increase of the

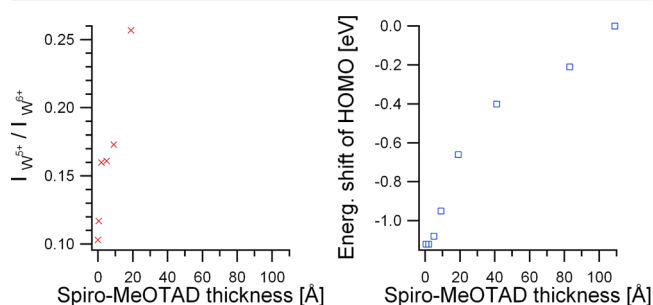


Figure 12. The W^{5+}/W^{6+} intensity ratio in the $W4f$ spectra and the shift of Spiro-MeOTAD HOMO binding energy at WO_3 /Spiro-MeOTAD interfaces. The relative intensity of the low energy shoulder labeled $W4f^{5+}$ in Figure 11 increases with increasing space charge. The HOMO energy shift corresponds to the electron transfer from Spiro-MeOTAD to WO_3 .

reduced $W4f$ species along with the binding energy shift of the HOMO with increasing Spiro-MeOTAD thickness. At the interface to the WO_3 substrate, a band bending of 1.12 eV is induced in Spiro-MeOTAD. The fact that no band bending is observed in the WO_3 film can be explained by Fermi level pinning to $W5d$ gap states. As the work function changes by

1.99 eV, a dipole formation at the interface of 0.87 eV is indicated.

In parallel to the HOMO the C1s core level line shown in Figure 13 shifts by 1.12 eV with a final binding energy position

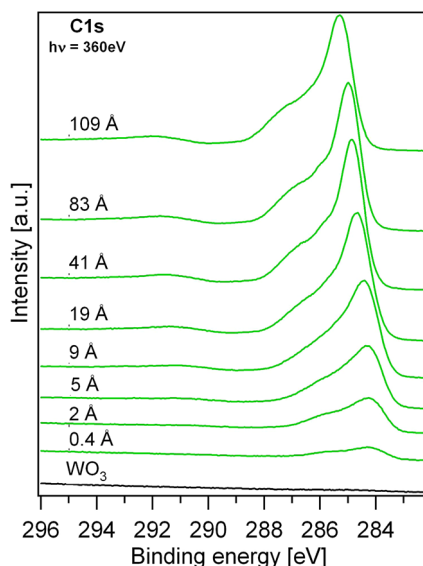


Figure 13. The C1s core level spectra of the stepwise evaporated Spiro-MeOTAD (green) on WO_3 (bottom-black). The C1s emission shifts (in parallel to the HOMO, see Figure 10) to higher binding energy values, indicating band bending up toward the WO_3 /Spiro-MeOTAD interface. The spectra were taken with a photon energy of 360 eV.

of the maximum at 285.25 eV. The core level line shape varies with increasing Spiro-MeOTAD thickness as evidenced in the background-subtracted C1s emissions displayed in Figure 14.

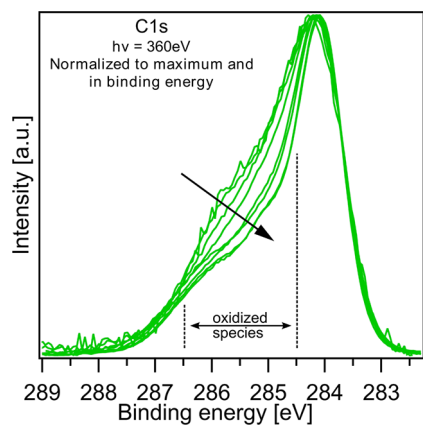


Figure 14. The background-subtracted C1s emissions normalized to intensity and in binding energy; toward the interface, the emission in the range of the oxidized C species (see Figure 2) is increased and decreases with growing Spiro-MeOTAD thickness. Spectra were recorded with a photon energy of 360 eV.

For direct comparison of the line shape, the spectra have been normalized to intensity and in binding energy. In the range from 284.5 to 286.5 eV, a decrease in intensity with growing Spiro-MeOTAD thickness is evident. As indicated in Figure 2, this binding energy range coincides with oxidized carbon species. Therefore, at first glance the increased relative intensity in the first Spiro-MeOTAD deposition steps could be

interpreted as a chemical oxidation of Spiro-MeOTAD reacting with tungsten oxide. However, in general, at reactive organic or inorganic semiconductor heterojunctions, band bending is not observed because of Fermi level pinning at interface states created by the reaction. Therefore, we tentatively correlate the increased relative C1s emission in the broad oxidized binding energy region at the interface to an intramolecularly localized hole charge resulting from electron transfer to WO_3 to form the strong interface dipole of 0.87 eV. The negative charge of the interface dipole and the negative charge from the Spiro-MeOTAD space charge region add to the W4f intensity assigned to W^{5+} . The electronic characteristics of the WO_3 /Spiro-MeOTAD contact are summarized in the interface band diagram sketched in Figure 15.

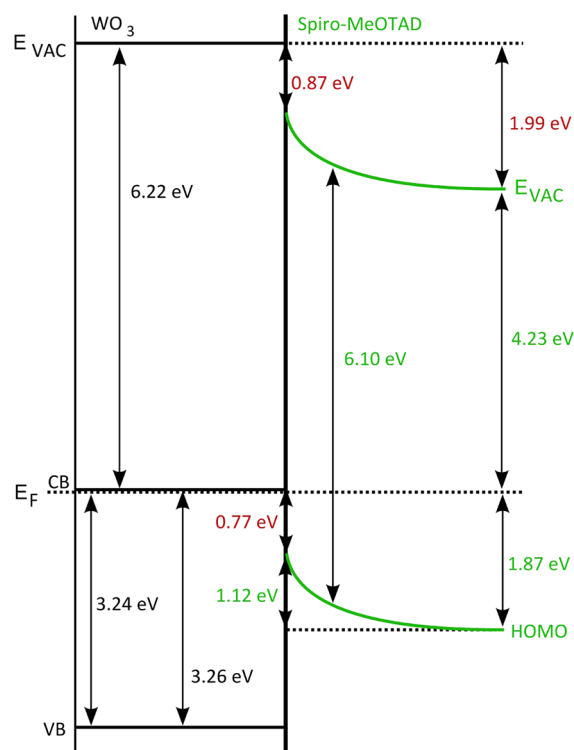


Figure 15. The band diagram of the WO_3 /Spiro-MeOTAD interface as formed for PVD of Spiro-MeOTAD onto a WO_3 film on TiO_2 . The difference between the measured work function change of 1.99 eV and the measured band bending of 1.12 eV in Spiro-MeOTAD is assigned to an interface dipole of 0.87 eV. The HOMO binding energy values refer to the photoemission maximum position.

Spiro-MeOTAD/ WO_3 . For the application of WO_3 as a hole injection layer, we also measured the Spiro-MeOTAD/ WO_3 interface band diagram by a stepwise WO_3 deposition onto a Spiro-MeOTAD film. As these experiments were performed at beamline TGM7 with maximal photon energy of 120 eV, the C1s core level could not be measured. Following the HOMO position of Spiro-MeOTAD in the first WO_3 deposition steps and the W4f position later on, a band bending of up to 1.17 eV was measured (Figures 16–18).

As in the reversed experiment described above, we assume Fermi level pinning in WO_3 and assign the shifts to a band bending in Spiro-MeOTAD. The total W4f shift, after extrapolation to 0 Å (shown in Figure 17), is equal to that of the Spiro-MeOTAD HOMO. Hereby, the W4f core level follows the shift of the Spiro-MeOTAD substrate. Also a

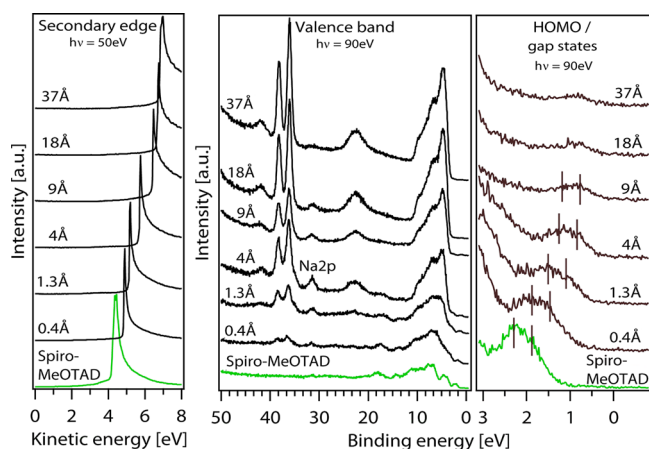


Figure 16. The secondary electron emission edge, valence band, and W4f core level spectra as well as the detailed HOMO/gap-state region of Spiro-MeOTAD (green-bottom) and the stepwise evaporated WO₃ of indicated thickness (black). The work function changes from 4.24 eV of Spiro-MeOTAD to 6.76 eV of WO₃. With growing WO₃ thickness, the Spiro-MeOTAD features are damped and the WO₃ features grow in intensity. The marked HOMO and HOMO-1 emission maxima of Spiro-MeOTAD shift to lower binding energy indicating induced band bending up toward the interface. In the two topmost spectra, the Spiro-MeOTAD HOMO emission is completely damped and the emission corresponds to W⁵⁺. Valence band spectra were taken with a photon energy of 90 eV and secondary edge measurements with a photon energy of 50 eV.

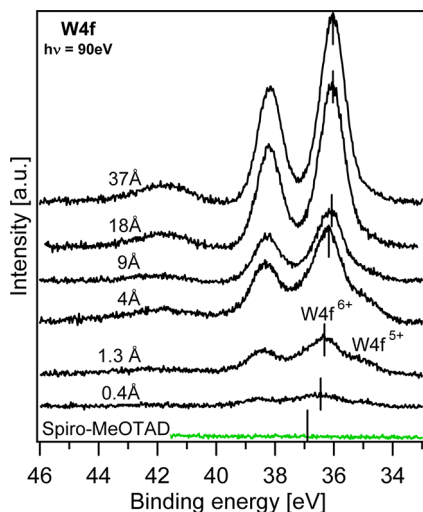


Figure 17. The W4f detailed measurements of Spiro-MeOTAD/WO₃ interfaces with the indicated formal WO₃ thickness. The decrease in the relative intensity of the low energy component is evident. The W4f emissions follow the shift of the Spiro-MeOTAD substrate. The spectra were taken with a photon energy of 90 eV.

reduced W4f⁵⁺ component is observed at the interface that disappears with WO₃ thickness, which becomes evident in the Shirley background-subtracted W4f detail spectra (Figure 17). In the first deposition step, the W⁵⁺/W⁶⁺ ratio is 0.29. An additional emission line appearing at 31.5 eV is attributed to sodium, which is part of the precursor used to prepare the TiO₂ substrate material. It has been shown that Na diffuses to the TiO₂ surface by thermal activation.^{23,24} So we assume that Na originates from the TiO₂ substrate and diffuses through Spiro-MeOTAD activated by the heat of the WO₃ source (1100 °C).

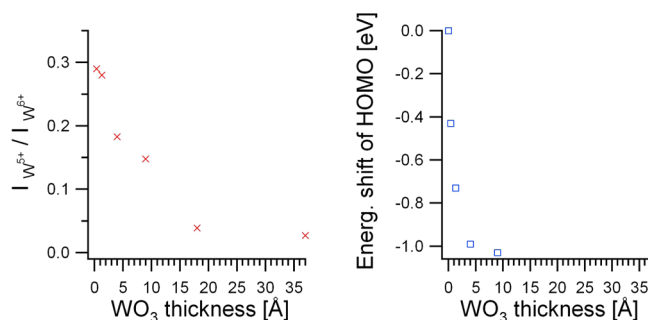


Figure 18. The W⁵⁺/W⁶⁺ intensity ratio in W4f spectra and shift of Spiro-MeOTAD HOMO binding energy at Spiro-MeOTAD/WO₃ interfaces with increasing formal WO₃ thickness. The relative intensity of the low energy shoulder labeled W4f⁵⁺ increases along with increasing space charge in Spiro-MeOTAD. The HOMO energy shift corresponds to an electron transfer from Spiro-MeOTAD to WO₃.

The electronic structure of the Spiro-MeOTAD/WO₃ interface is summarized in Figure 19. The work function

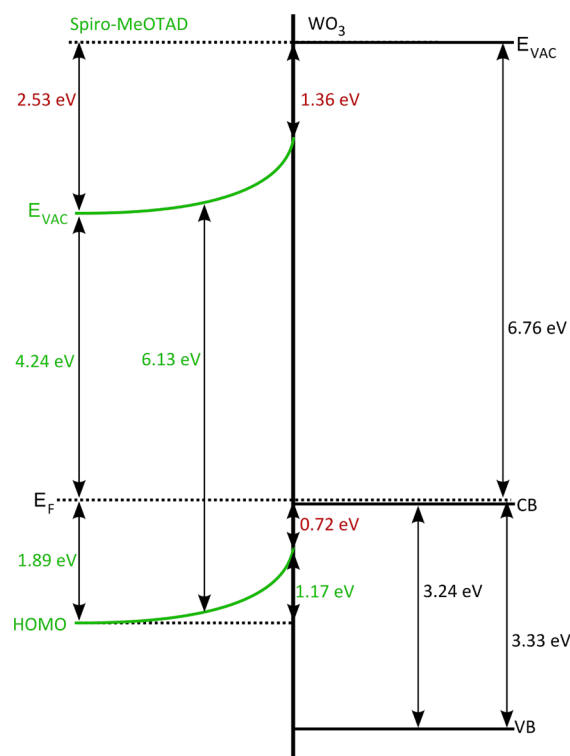


Figure 19. The band diagram of the Spiro-MeOTAD/WO₃ interface as formed for PVD of WO₃ onto a film of Spiro-MeOTAD. The difference of the measured work function change of 2.53 eV and the measured band bending of 1.17 eV in Spiro-MeOTAD is assigned to an interface dipole of 1.36 eV. The lineup of the Spiro-MeOTAD HOMO maximum with the WO₃ conduction band is 0.72 eV, very similar to the 0.77 eV measured in the reverse deposition sequence (Figure 15).

changes from 4.24 of the Spiro-MeOTAD surface to 6.76 eV after WO₃ deposition. A 1.17 eV portion of the work function difference of 2.53 eV is supplied by the band bending in the space charge region in Spiro-MeOTAD. The remaining 1.36 eV is assigned to an interface dipole.

DISCUSSION

The striking similarity between the valence band spectra of the drop-casted Spiro-MeOTAD films prepared under inert gas atmosphere and transferred to UHV without contact to ambient atmosphere and the in situ-prepared films by Spiro-MeOTAD evaporation in UHV demonstrates the equivalency of the two deposition methods with respect to the electronic structure.

In the vacuum level alignment of the pristine materials, the Spiro-MeOTAD HOMO maximum is found 0.64 eV above the conduction band minimum of the almost defect-free WO₃ and 0.01 eV above the oxygen-defective WO₃ that has been reduced by the oxygen-defective TiO₂. At the experimental WO₃/Spiro-MeOTAD and Spiro-MeOTAD/WO₃ contacts, the HOMO is found 0.77 and 0.72 eV below the WO₃ conduction band, respectively, and band bending due to positive space charge in Spiro-MeOTAD of 1.12 and 1.17 eV is induced. Thus, the lineup and band bending seem to be independent of the initial and final work function of WO₃ of 6.22 and 6.76 eV, respectively, in the two deposition sequences. The shift of the Spiro-MeOTAD HOMO below the WO₃ conduction band is caused by, respectively, formation of interface dipoles of 0.87 and 1.36 eV, which compensates for the different WO₃ work functions. The doping limit in the Spiro-MeOTAD:WO₃ composites is similar to the band bending values measured at the interfaces. Therefore, we assume, respectively, precipitation of WO₃ and a similar band lineup at internal interfaces and charge transfer as measured in the bilayer experiments.

In the composites and at the interfaces we find an increased emission of a low binding energy W4f component in WO₃ labeled with the formal oxidation state W⁵⁺. The maximum W⁵⁺ to W⁶⁺ ratios obtained for the Spiro-MeOTAD/WO₃ (0.29) and WO₃/Spiro-MeOTAD (0.26) interface experiments are in good agreement with the ratios (0.26) obtained for composites in the maximum reduced regime with WO₃ content of 34% and below. Thus, we believe that the W4f⁵⁺ component is correlated to the electrons transferred from Spiro-MeOTAD to WO₃ corresponding to the space charge in Spiro-MeOTAD and the dipole at the Spiro-MeOTAD/WO₃ interfaces. In the WO₃/Spiro-MeOTAD case performed at the undulator beamline, we could also measure the C1s orbital. Increased emission in the binding energy range corresponding to oxidized carbon species was measured. No such additional C1s emission was observed for Spiro-MeOTAD deposited onto TiO₂ (not shown), where the interface dipole is small (ca. 0.2 eV). As in general at reactive semiconductor heterojunctions, no band bending can be observed because of the formation of defect states in the semiconductor energy gap. This was explicitly shown by Prietsch et al.²⁵ for reactive p- and n-GaAs surfaces, which show a common Fermi-level position at the Na/GaAs interface and by Mayer et al. for Br₂ on n-InSe, which show band bending for nonreacted Br₂ on n-InSe and no band bending after a reaction was activated by synchrotron radiation.²⁶ In addition, the difference spectra (not shown here) of O2s emissions, located at ca. 27.9 eV binding energy, show the same line shape and, thus, no hint of a chemical reaction, neither for the composites nor for the WO₃/Spiro-MeOTAD interface. The difference spectra were obtained by subtracting the pristine WO₃ spectra from the respective spectra. Therefore, we exclude a chemical oxidation reaction with oxygen breaking bonds to WO₃ and forming bonds to carbon in the Spiro-MeOTAD molecule. We tentatively correlate the additional C1s emission at the interface

to the positive charge of the interface dipole and assume that this charge is localized on parts of the Spiro-MeOTAD molecules closest to WO₃, giving rise to an increased relative emission in the oxidized C1s binding energy region.

In a simple model, we assume the WO₃ to consist of W₃O₉ clusters, the smallest species that can be considered as a molecular model for bulk WO₃ from an electronic structure and chemical point of view. The transferred integer electron charge is shared between three W atoms that form the HOMO of negatively charged W₃O₉[−] clusters,²⁷ leading to a partial charge corresponding to the charge transfer-induced W species in the formal oxidation state 5+. Assuming the charged clusters to be homogeneously distributed among neutral clusters, the number of transferred integer charges per square centimeter (*Q*) of each deposition step in the Spiro-MeOTAD/WO₃ bilayer experiments is given as

$$Q = \frac{1}{3} \times \frac{\varphi d}{V_{\text{mol}}} \quad (1)$$

where *d* is the formal WO₃ thickness, φ the respective W4f⁶⁺ to W4f⁵⁺ ratio, and *V*_{mol} the molar volume of WO₃. The factor 1/3 stems from the above given argument that W₃O₉ clusters may have one integer electron charge. The areal charge density is highest ($6.63/3 \times 10^{13} \text{1/cm}^2$) for a formal WO₃ thickness of 9 Å, which roughly corresponds to the W₃O₉ cluster size (Figure 20).²⁷

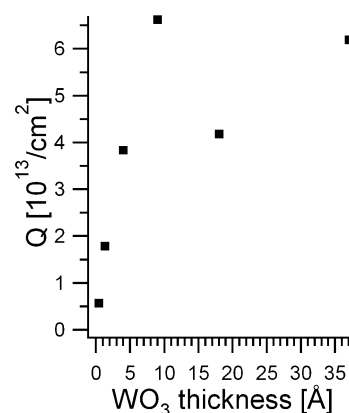


Figure 20. The calculated areal density of charges in WO₃ at the Spiro-MeOTAD/WO₃ interface with increasing formal WO₃ thickness.

SUMMARY

In this paper it is shown that the synchrotron-induced valence band photoelectron spectra of Spiro-MeOTAD prepared by drop-casting from chlorobenzene solution under inert gas atmosphere and by in situ evaporation are almost identical, proving that evaporated Spiro-MeOTAD may be used as an in situ model for drop-casted Spiro-MeOTAD. The p-doping of Spiro-MeOTAD by coevaporation with the transition metal oxide WO₃ and the formation of a positively charged space charge region in Spiro-MeOTAD at the WO₃/Spiro-MeOTAD and Spiro-MeOTAD/WO₃ interfaces is shown. The maximum Fermi level shift of 0.98 eV in Spiro-MeOTAD:WO₃ composites corresponds well to the Fermi level shift of 1.12 and 1.17 eV at the WO₃/Spiro-MeOTAD and Spiro-MeOTAD/WO₃ interfaces. The work function of a pristine Spiro-MeOTAD film is measured to be 4.23 eV, while the work function of WO₃ is 6.76 eV for a thick layer showing little

emission of a $W4f^{5+}$ component and 6.13 eV for WO_3 on TiO_2 where strong W^{5+} emission is found. In the interface experiments, a dipole formation of 0.87 eV is shown for Spiro-MeOTAD deposited onto WO_3 and of 1.36 eV for WO_3 deposited onto Spiro-MeOTAD.

The different dipole values compensate for the different WO_3 work functions so that a similar lineup of the Spiro-MeOTAD HOMO and the WO_3 conduction band of 0.72 and 0.77 eV is found. At the interface to Spiro-MeOTAD we find a low binding energy $W4f$ component and an increased emission of the C1s orbital in the binding energy range corresponding to oxidized carbon species. We tentatively correlate the W^{5+} emission with the charge transferred from the space charge region in Spiro-MeOTAD and the charge transferred to form the interface dipole. In a simple model, a area density of around $6.63 \times 10^{13} \text{1/cm}^2$ has been calculated to reside in the W^{5+} species. We tentatively correlate the additional C1s emission at the interface to the positive charge of the interface dipole and assume that this charge is localized on parts of the Spiro-MeOTAD molecules closest to WO_3 .

AUTHOR INFORMATION

Corresponding Author

*E-mail: mayerth@tu-darmstadt.de.

Notes

The authors declare no competing financial interest.

ACKNOWLEDGMENTS

We acknowledge our cooperation partner BASF within the OPEG 2010 project funded by the BMBF within the organic photovoltaic initiative. Special thanks go to the group of Christian Pettenkofer and to the BESSY staff for their support at BESSY II.

REFERENCES

- (1) Chan, C. K.; Zhao, W.; Kahn, A.; Hill, I. G. *Appl. Phys. Lett.* **2009**, *94*, 203306.
- (2) Bach, U.; Lupo, D.; Comte, P.; Moser, J. E.; Weissörtel, F.; Salbeck, J.; Spreitzer, H.; Grätzel, M. *Nature* **1998**, *395*, 583–585.
- (3) Crispin, A.; Crispin, X.; Fahlman, M.; dos Santos, D. A.; Cornil, J.; Johansson, N.; Bauer, J.; Weissörtel, F.; Salbeck, J.; Bredas, J. L.; et al. *J. Chem. Phys.* **2002**, *116*, 8159–8167.
- (4) Johansson, N.; dosSantos, D. A.; Guo, S.; Cornil, J.; Fahlman, M.; Salbeck, J.; Schenk, H.; Arwin, H.; Bredas, J. L.; Salaneck, W. R. *J. Chem. Phys.* **1997**, *107*, 2542–2549.
- (5) Pudlich, R.; Fuhrmann-Lieker, T.; Salbeck, J. *Adv. Polym. Sci.* **2006**, *199*, 83–142.
- (6) Snaith, H. J.; Grätzel, M. *Appl. Phys. Lett.* **2006**, *89*, 26114.
- (7) Kroger, M.; Hamwi, S.; Meyer, J.; Riedl, T.; Kowalsky, W.; Kahn, A. *Org. Electron.* **2009**, *10*, 932–938.
- (8) Ha, S. D.; Meyer, J.; Kahn, A. *Phys. Rev. B* **2010**, *82*, 155434.
- (9) Meyer, J.; Hamwi, S.; Schmale, S.; Winkler, T.; Johannes, H. H.; Riedl, T.; Kowalsky, W. *J. Mater. Chem.* **2009**, *19*, 702–705.
- (10) Hein, C.; Mankel, E.; Mayer, T.; Jaegermann, W. *Phys. Status Solidi A* **2009**, *206*, 2757–2762.
- (11) Shirley, D. A. *Phys. Rev. B* **1972**, *5*, 4709–4714.
- (12) Mašek, K.; Nemšák, S.; Mravčáková, M.; Blumentrit, P.; Skála, T.; Škoda, M.; Matolín, V. *J. Phys. Conf. Ser.* **2008**, *100*, 012008.
- (13) Mašek, K.; Libra, J.; Skála, T.; Cabala, M.; Matolín, V.; Cháb, V.; Prince, K. C. *Surf. Sci.* **2006**, *600*, 1624–1627.
- (14) Dixon, R. A.; Williams, J. J.; Morris, D.; Rebane, J.; Jones, F. H.; Eggedell, R. G.; Downes, S. W. *Surf. Sci.* **1998**, *399*, 199–211.
- (15) Schwanitz, K.; Mankel, E.; Hunger, R.; Mayer, T.; Jaegermann, W. *Chimia* **2007**, *61*, 796–800.
- (16) Richter, J. H.; Henningsson, A.; Sanyal, B.; Karlsson, P. G.; Andersson, M. P.; Uvdal, P.; Siegbahn, H.; Eriksson, O.; Sandell, A. *Phys. Rev. B* **2005**, *71*, 235419.
- (17) Wriedt, H. J. *Phase Equilib.* **1989**, *10*, 368–383.
- (18) Patel, K. J.; Panchal, C. J.; Kheraj, V. A.; Desai, M. S. *Mater. Chem. Phys.* **2009**, *114*, 475–478.
- (19) Ottaviano, L.; Maccallini, E.; Santucci, S. *Surf. Sci.* **2001**, *492*, L700–L704.
- (20) Antonaia, A.; Polichetti, T.; Addonizio, M. L.; Aprea, S.; Minarini, C.; Rubino, A. *Thin Solid Films* **1999**, *354*, 73–81.
- (21) Mašek, K.; Blumentrit, P.; Beran, J.; Skála, T.; Piš, I.; Libra, J.; Matolín, V. *Surf. Interface Anal.* **2010**, *42*, 540–544.
- (22) Morar, J. F.; Himpsel, F. J.; Hughes, G.; Jordan, J. L.; Mcfeely, F. R.; Hollinger, G. *J. Vac. Sci. Technol., A* **1985**, *3*, 1476–1480.
- (23) Feng, X. J.; Hock, R.; Mankel, E.; Lingenfeller, D.; Volker, B.; Mayer, T.; Jaegermann, W. *J. Phys. Chem. C* **2010**, *114*, 20049–20054.
- (24) Kosuge, K. *Chemistry of Non-Stoichiometric Compounds*; Oxford University Press: Oxford, 1994.
- (25) Prietsch, M.; Laubschat, C.; Domke, M.; Kaindl, G. *Europhys. Lett.* **1988**, *6*, 451–456.
- (26) Mayer, T.; Lehmann, J.; Pettenkofer, C.; Jaegermann, W. *Chem. Phys. Lett.* **1992**, *198*, 621–627.
- (27) Huang, X.; Zhai, H. J.; Li, J.; Wang, L. S. *J. Phys. Chem. A* **2006**, *110*, 85–92.